Tellus SERIES A DYNAMIC METEOROLOGY AND OCEANOGRAPHY
PUBLISHED BY THE INTERNATIONAL METEOROLOGICAL INSTITUTE IN STOCKHOLM

Tellus (2010), 62A, 298–318
Printed in Singapore. All rights reserved

© 2010 The Authors
Journal compilation © 2010 Blackwell Munksgaard

TELLUS

Mesoscale satellite data assimilation: impact of cloud-affected infrared observations on a cloud-free initial model state

By CURTIS J. SEAMAN[1]*, MANAJIT SENGUPTA[2] and THOMAS H. VONDER HAAR[1],
[1]*Department of Atmospheric Science, Colorado State University, Fort Collins, CO, USA;* [2]*Cooperative Institute for Research in the Atmosphere, Colorado State University, Fort Collins, CO, USA*

(Manuscript received 24 July 2009; in final form 14 January 2010)

ABSTRACT

This work presents the results of assimilating cloud-affected radiances from geostationary, infrared window and water vapour channels into a mesoscale, cloud-resolving model using a four-dimensional variational assimilation system for the case of an altocumulus cloud over the Great Plains of the United States. In this case, the initial model state, based on reanalysis data, was virtually cloud-free. The impacts of cloudy-scene radiances on a cloud-free model state (and, more generally, accurate satellite observations on inaccurate model initial conditions) in a four-dimensional variational assimilation framework are discussed. Results indicate that, in a cloud-free model state, the assimilation of cloudy radiances modifies the initial conditions as if no cloud exists. This results in a cooling of the surface and lower troposphere upon assimilation of infrared window channels, and an increase in mid- to upper tropospheric humidity upon assimilation of water vapour channels in an attempt to minimize the differences between the modelled and observed radiances. Neither modification of the initial conditions leads to the formation of the observed cloud. The size of the domain and the background error covariance are found to have a significant impact on the results.

1. Introduction

Over the past twenty years, there has been a dramatic increase in the amount and types of satellite data assimilated by operational forecast centres (Weng, 2007). Satellite observations of the land, ocean and atmosphere cover the breadth of the electromagnetic spectrum and are used to provide information on pressure, temperature, winds, humidity, aerosols, chemistry and a variety of cloud properties (Kidder and Vonder Haar, 1995). These observations comprise the majority of data ingested into numerical weather prediction (NWP) models (Weng, 2007).

Numerous studies have shown a benefit to assimilating humidity information from infrared (IR) satellite sensors (McNally and Vespirini, 1996; Ruggiero et al., 1999; McNally et al., 2000; Raymond et al., 2004; Fan and Tilley, 2005), microwave sensors (Hoffman et al., 1990; Wu et al., 1995; Zapotocny et al., 2002; Marécal and Mahfouf, 2002; Deblonde and English, 2003; Benjamin et al., 2004) and, more recently, Global Positioning System (GPS) satellites (Ha et al., 2003; Cucurull et al., 2008). However, in the studies referenced above, assimilation of IR observations of humidity has typically been limited to areas not affected by cloud (effectively and henceforth termed, ‘cloud-free’). Assimilation of microwave radiances has typically been limited to cloud-free areas over the ocean due, not only to attenuation of the signal by clouds and precipitation (Weng, 2007), but also to poorly known land surface emissivities (Ruston and Vonder Haar, 2004). The limitation of assimilating satellite humidity information in cloud-free areas is a significant one, considering that clouds cover more than half of the globe (Warren et al., 1986, 1988; Mokhov and Schlesinger, 1993; Rossow and Dueñas, 2004).

Assimilation of satellite data in cloudy areas has been performed using visible, infrared and microwave sensors (Lipton, 1993; Garand and Hallé, 1997; Tomassini et al., 1999; Marécal and Mahfouf, 2002; Yucel et al., 2003; Moreau et al., 2004; Bauer et al., 2006; Deblonde et al., 2007; Weng et al., 2007; Benedetti and Janisková, 2008). These studies have assimilated retrievals of cloud and/or atmospheric properties from satellites and not the direct satellite radiances. The assimilation of retrievals introduces an additional source of error—namely,

---

*Corresponding author.
Department of Atmospheric Science, Colorado State University, Fort Collins, CO 80523-1371, USA.
e-mail: seaman@cira.colostate.edu
DOI: 10.1111/j.1600-0870.2010.00436.x

error in the retrieval—over direct radiance assimilation that must be accounted for (Kalnay, 2003). Direct assimilation of cloud-affected radiances has been performed previously (Vukićević et al., 2004, 2006; McNally, 2009) and is an active area of research.

Direct radiance assimilation in cloud-affected scenes in a mesoscale model is a complicated problem but, as discussed in Vukićević et al. (2006), it is possible given the following considerations:

(1) The forward model must be able to resolve cloud scale motions.[1] Cloud resolving models typically have large state vectors with poorly quantified uncertainties and are computationally expensive.

(2) The assimilation of satellite radiance data in cloudy scenes requires the use of a radiative transfer model of sufficient complexity to resolve the interaction of clouds and radiation on the scales needed for item 1 for the broad range of wavelengths used by environmental satellites.

(3) Temporal consistency must be maintained during the assimilation over the period of cloud evolution, given the high temporal variability of cloud properties. This requires the development and use of a full adjoint of the cloud resolving model, or another similar 'smoothing data assimilation method' (van Leeuwen, 2001). This is difficult to implement and is also computationally expensive.

(4) The error statistics necessary for optimal implementation of variational assimilation techniques are not well known as cloud resolving models have not been systematically compared with satellite radiance observations.

(5) Independent verification data are required to evaluate the accuracy of the results and to better quantify the information content of the satellite data.

The Regional Atmospheric Modeling Data Assimilation System (RAMDAS, Zupanski et al., 2005) was developed specifically to address these issues and to allow for research into the impact of both clear and cloud-affected visible and infrared satellite radiance observations in a mesoscale forecast model. RAMDAS will be discussed in more detail in Section 2. Items 2, 3 and 5 have been addressed in Greenwald et al. (2002, 2004) and Vukićević et al. (2004, 2006). The present work contributes to item 5 and provides insight on the impact of the error statistics and uncertainties listed in items 1 and 4.

In Vukićević et al. (2006), the IR window channels from the GOES[2] Imager instrument in a cloudy scene were assimilated using RAMDAS for a case of cirrus clouds over the Great Plains of the United States. In that case, the initial model state contained cirrus clouds and the characterization of the clouds was improved after assimilation of the satellite data. The present study extends that work by assimilating GOES Imager and Sounder window and water vapour channels in a cloudy scene for a case of an altocumulus cloud, also over the Great Plains, except that this cloud is not present in the initial model state. The impact of cloud-affected satellite data on a cloud-free initial model state is discussed.

Altocumulus and altostratus clouds are often underpredicted by NWP models (Illingworth et al., 2007). It is attractive to explore whether the addition of satellite observations of the clouds and/or water vapour above and near the clouds would improve the predictive skill of the models for these cloud types. As these clouds are often underpredicted, it is often the case that the initial model state does not contain cloud when satellite observations indicate a cloud is present. Such a case is presented here. It is therefore necessary to observe and investigate the behaviour of the assimilation system when this type of discrepancy exists between the model and the observations.

The goals of this study are as follows: (1) explore the use of cloud-affected radiance data in a cloud-free initial forward model run, (2) quantify the impact of infrared water vapour and window channel data on the initial temperature and dew point profiles, (3) compare and contrast the impact of GOES Imager versus GOES Sounder data for similar channels and (4) compare and contrast the impact of using only water vapour channels versus using water vapour plus window channels.

The remainder of the paper is as follows. Details of RAMDAS are presented in Section 2. A description of the case study and the experiment set-up are given in Section 3. The results of the experiments are presented in Section 4. Section 5 discusses the sensitivity of the results to various model and/or assimilation parameters, including domain size, decorrelation length and variance (components of the background error covariance matrix), and the use of additional IR channels. A discussion of the conclusions and possible future work follows in Section 6.

2. Regional Atmospheric Modeling Data Assimilation System

The RAMDAS was developed at Colorado State University with a primary emphasis on the assimilation of satellite radiance data in both clear and cloudy conditions. This system is based on the Regional Atmospheric Modeling System (RAMS; Tripoli and Cotton, 1982; Pielke et al., 1992; Cotton et al., 2003) model—a non-hydrostatic, mesoscale, cloud resolving, primitive equation model—with full adjoint, a visible and infrared observational operator (VISIROO) designed to handle both clear and cloudy radiative transfer, and a computationally efficient 4-DVAR

---

[1] It should be noted that McNally (2009) developed a methodology for the assimilation of cloud-top pressure and cloud fraction from IR radiances that does not require high horizontal model resolution. The present work, in contrast, uses a control variable that contains microphysical quantities (e.g. pristine ice water content), which necessitates the use of a cloud-resolving model.

[2] Geostationary Operational Environmental Satellite (Menzel and Purdom, 1994).

minimization algorithm based on the Eta Data Assimilation System (EDAS; Zupanski et al., 2002). A brief overview of RAMDAS and each of its components follows. Further details of RAMDAS can be found in Zupanski et al. (2005).

For these experiments RAMDAS was set up to minimize the 4-DVAR cost function, $J(\vec{\mathbf{x}}_0)$, given by:

$$J(\vec{\mathbf{x}}_0) = \frac{1}{2}\left(\vec{\mathbf{x}}_0 - \vec{\mathbf{x}}_b\right)^T \mathbf{B}^{-1}\left(\vec{\mathbf{x}}_0 - \vec{\mathbf{x}}_b\right) + \frac{1}{2}\sum_t \left\{H[M_t(\vec{\mathbf{x}}_0)] - \vec{\mathbf{y}}_t\right\}^T \mathbf{R}_t^{-1}\left\{H[M_t(\vec{\mathbf{x}}_0)] - \vec{\mathbf{y}}_t\right\} \quad (1)$$

where $\vec{\mathbf{x}}_0$ is the initial model state vector, or control variable in this case. In each term, superscript T represents the transpose operator. The control variable includes pressure, temperature, horizontal and vertical winds, total water mixing ratio, and the water mixing ratios of six cloud/precipitation types: rain, hail, snow, graupel, pristine ice and aggregates. The first term in (1) represents the difference between the initial model state vector and the background (first guess or previous iteration) state vector, $\vec{\mathbf{x}}_b$, weighted by the inverse of the background error covariance matrix, **B**. The second term is the sum of the differences between the model states, $M_t(\vec{\mathbf{x}}_0)$ and the observations, $\vec{\mathbf{y}}_t$, for all observation times, t, weighted by the inverse of the observation error covariance matrix, $\mathbf{R}_t$. The observation error covariance matrix varies with time only to allow for the possibility of assimilating different observations (satellite channels) at different times. As discussed in Section 3, the observation error covariance for each channel is considered time-invariant. M is the non-linear forward model that integrates the initial state vector $\vec{\mathbf{x}}_0$ forward to time t. H is the observational operator that maps the forward model state into the observation space (i.e. the radiative transfer model that converts the model output to brightness temperatures). Additional information about the background and observation error covariance matrices is given in Section 3.

Previous studies utilizing RAMDAS have included a gravity wave penalty term and/or model error term (Zupanski et al., 2005; Vukićević et al., 2006). The model error was previously represented as a linear forcing for each of the prognostic variables contained in $\vec{\mathbf{x}}_0$ with temporal variability represented as a Markov process with systematic and random components (Zupanski, 1997). However, Vukićević et al. (2006) concluded the following: (1) this characterization of the model error produced instabilities in the model solution, (2) it was unable to account for gross errors due to a lack of constraint by observations in cloudy scenes and with large lateral boundary condition errors and (3) that the results were of sufficient quality without compensating for model error. Gravity waves may be important in altocumulus dynamics (Seaman and Vonder Haar, 2003), so the gravity wave penalty was left off so as to not filter them out (Zupanski et al., 2005).

Minimization of the cost function (1) is achieved by calculating the gradient of the cost function with respect to the control variable at the initial time, and finding where the gradient is nearly equal to zero. Since **B** and **R** are symmetric, this gives

$$\frac{\partial J}{\partial \vec{\mathbf{x}}_0} = \mathbf{B}^{-1}\left(\vec{\mathbf{x}}_0 - \vec{\mathbf{x}}_b\right) + \sum_t \mathbf{M}^T \mathbf{H}^T \mathbf{R}_t^{-1}\{H[M_t(\vec{\mathbf{x}}_0)] - \vec{\mathbf{y}}_t\} \approx 0, \quad (2)$$

where $\mathrm{H} = \frac{\partial H}{\partial M(\vec{\mathbf{x}}_0)}$ represents the tangent linear model of the observational operator and $\mathbf{M} = \frac{\partial M}{\partial \vec{\mathbf{x}}_0}$ represents the tangent linear model of the forward model.

There is no analytical solution for finding the initial model state vector that solves (2). The solution must be estimated by searching the gradient defined by (2) in control variable space using an iterative algorithm (Kalnay, 2003). RAMDAS uses the limited memory quasi-Newton algorithm of Nocedal (1980). For faster convergence of the minimization, a Hessian preconditioning algorithm is used (Zupanski, 1993, 1996; Zupanski et al., 2005). The preconditioning algorithm utilizes a change of variable that allows the minimization algorithm to come closer to the centre of the cost function minimum after each iteration. The minimization algorithm stops when either the change in cost function between iterations is sufficiently small (convergence) or the maximum number of iterations has been achieved. Convergence monitoring and the restart procedure are based on the angle test of Shanno (1985).

A schematic of RAMDAS is presented in Fig. 1. The forward NWP model (M in eq. 1) is the RAMS model. Clouds and precipitation are explicitly represented by a microphysical parametrization that utilizes a one-moment cloud liquid water scheme (Walko et al., 1995) and a two-moment rain and ice particle (snow, hail, graupel, pristine ice and aggregates) scheme (Meyers et al., 1997). RAMS is coupled with the Land Ecosystem Atmosphere Feedback model (LEAF-2; Walko et al., 2000), which accounts for feedbacks between the atmosphere and the surface soil and vegetation. Radiative fluxes are parametrized using the two-stream approach developed by Harrington (1997).

RAMDAS utilizes version 4.2.9 of the RAMS code, which has been 'frozen' for the development of a full RAMS adjoint. The adjoint [the transpose of the tangent linear model, $\mathbf{M}^T$ in (2)] is an adjoint of the true tangent linear model of the RAMS discrete algorithm—including moist physics and microphysical processes—except that radiative and convective parametrizations have not been included. The effects of radiation are assumed to be of secondary importance over the short time scales of RAMDAS assimilation experiments, and the convective parametrization is not needed at the spatial resolution used for cloudy scene data assimilation, where cloud processes can be explicitly resolved. An adjoint of the LEAF-2 model is included. Additional details of the RAMS adjoint are discussed in Zupanski et al. (2005).

The visible and infrared observational operator (VISIROO) and its adjoint (H and $\mathbf{H}^T$ in (2), respectively) consist of two radiative transfer models that convert the RAMS output to radiance at the wavelengths of the satellite observations. VISIROO

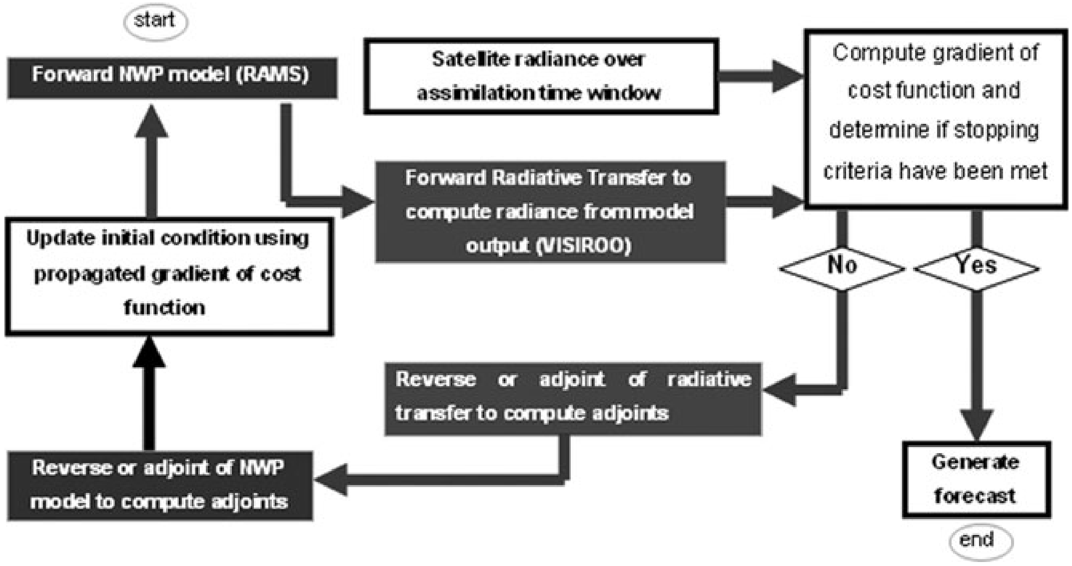

Fig. 1. Schematic of the RAMDAS algorithm. RAMDAS begins in the upper-left with the forward numerical weather prediction (NWP) model run (RAMS). The forward model output is converted to radiance via the operational operator (VISIROO), which is then compared to the satellite observations. The cost function and its gradients are calculated. The adjoints calculate the sensitivities of the model radiances to the control variables, which are then used to update the initial conditions of the forward model for the next iteration to minimize the cost function. When the change in the cost function value is small enough, the system exits with a final forecast based on these updated initial conditions.

was developed specifically for the GOES instruments. For visible wavelengths, VISIROO utilizes the Spherical Harmonic Discrete Ordinate Method (SHDOM; Evans, 1998). For infrared wavelengths, VISIROO uses a delta-Eddington approach (Deeter and Evans, 1998). Both of these models consider multiple scattering and assume a plane parallel atmosphere. Anomalous diffraction theory (Bryant and Latimer, 1969) is also used to estimate single scattering properties for all types of cloud and precipitation particles predicted by RAMS. Gaseous extinction is calculated using the Optical Path Transmittance (OPTRAN) method (McMillin et al., 1995).

The adjoint of the observational operator is based on the assumption of linearity within the forward radiative transfer models, which was found to hold for infrared wavelengths, but not for visible wavelengths (Greenwald et al., 2004). The visible channels of GOES are not used in this study. The observational operator and its adjoint are discussed in more detail in Greenwald et al. (2002) and Greenwald et al. (2004).

3. Experiment set-up

The present study was sponsored by the U.S. Department of Defense Center for Geosciences and Atmospheric Research (CGAR) for the purposes of improving forecasting of mid-level, mixed-phase clouds (i.e. altocumulus and altostratus). The occurrence of mid-level clouds is often underpredicted by NWP models (e.g. Illingworth et al., 2007). These clouds are important for a number of aviation and military applications (Fleishauer et al., 2002), which require accurate short-term (0–6 hour) forecasts. The need to improve understanding and forecasting of mid-level clouds led to the Cloud Layer Experiment (CLEX) program, a series of field experiments dedicated to understanding the dynamics and microphysics of non-frontal, non-orographic, mid-level clouds, primarily through aircraft and satellite observations.

The Ninth CLEX field experiment (CLEX-9) took place between 8 October and 4 November 2001. During CLEX-9, the University of Wyoming King Air research aircraft flew ten flight missions on eight different days through mid-level clouds over the western Great Plains of the United States (Carey et al., 2008). Ground-based measurements, including microwave, visible and infrared radiometers, lidar and radiosonde launches, were taken at North Platte, Nebraska (41.1°N latitude, 100.8°W longitude) throughout the experiment.

In this study, we focus on the altocumulus cloud that formed on 2 November 2001, and which passed directly over North Platte. Visible satellite imagery (Fig. 2) reveals that this cloud was isolated from other cloud systems. The lack of overrunning cirrus clouds in this case allows us to perform this type of assimilation experiment as Vukićević et al. (2006) demonstrated that infrared window channels are primarily only sensitive to the upper-most cloud layer in a given column. Also, the lack of other surrounding cloud features simplifies the dynamics that the model must reproduce.

During its mature phase, this altocumulus cloud was approximately 400 km × 200 km in horizontal extent and was less than 500 m thick. Aircraft observations presented in Carey et al. (2008) indicate this cloud existed as a supercooled liquid layer

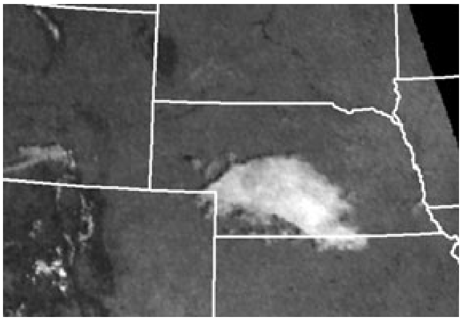

Fig. 2. GOES visible image (Imager channel 1) of the 2 November 2001 altocumulus cloud taken at 1445 UTC (0745 local time). Boundaries of the U.S. state of Nebraska and neighbouring states are shown.

that varied between 100 and 200 m thick above precipitating ice virga that extended 200–300 m below the liquid layer. Cloud base and cloud top, as measured by in situ microphysical probes, were 4.2 and 4.7 km above mean sea level (MSL), respectively. The reader is referred to Carey et al. (2008) for further details of the microphysical properties of this cloud and other mid-level clouds observed during CLEX-9.

To simulate this case, a 75 × 75 (horizontal) × 84 (vertical) grid was set up in RAMS, centred on North Platte, Nebraska (Fig. 3). Horizontal grid spacing was set at 6 km, which is near the lower limit for resolving cloud processes (Khairoutdinov and Randall, 2003). Vertical levels were determined using a stretched-z grid, beginning at 50 m for the lowest level, increasing by 3% per level, and capped at 1000 m in the stratosphere. Vertical resolution at the height of the aircraft-observed cloud is approximately 150 m, which is just sufficient to resolve a 500 m thick cloud. The total volume of the domain is 450 km × 450 km × 18 km. The size and resolution of this domain were chosen, in part, based on computational resource limitations. The impacts of varying the size of the domain are discussed in Section 5.

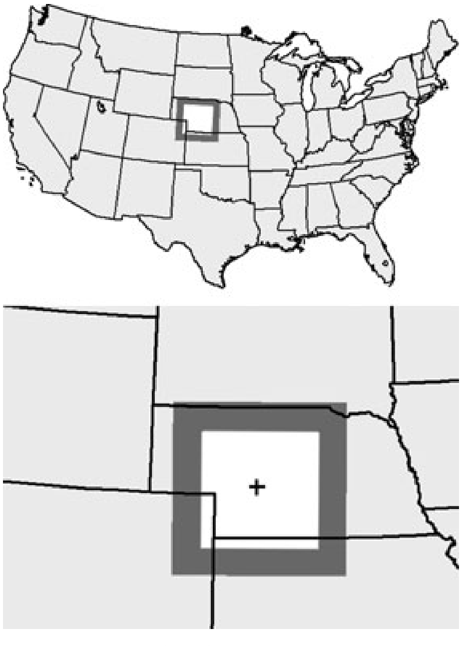

Fig. 3. Location and size of the forward/adjoint model grid. The dark shaded region represents the portion of the 450 km × 450 km grid excluded from the cost function calculation and, hence, is not directly modified by the assimilation. The cross in the lower panel represents the location of North Platte, Nebraska.

Lateral boundary condition errors are particularly large in cloudy-scene data assimilation and have a tendency to dominate the total cost (Vukićević and Paegle, 1989). Therefore, as in Vukićević et al. (2006), the lateral boundaries have been masked out of the cost function calculation (Fig. 3). The cost function is calculated (and the initial conditions are updated) only on the 50 × 50 domain at the centre of the grid, while the forward model and its adjoint are integrated over the entire 75 × 75 domain. Given the initial model horizontal wind speeds between 20 and 30 m s^{-1} in the mid-troposphere, and the short assimilation window (45 minutes, as discussed below), this ‘grid mask’ is sufficient to prevent nearly all lateral boundary condition errors from impacting the assimilation.

RAMDAS was run with three different sets of geostationary infrared satellite data: (1) GOES Imager window (channel 4, 10.7 μm) and water vapour (channel 3, 6.7 μm) channels, referred to as the ‘Imager experiment’; (2) GOES Sounder window (channel 7, 12.02 μm) and mid-level water vapour (channel 11, 7.02 μm) channels, referred to as the ‘Sounder experiment’ and (3) the two water vapour channels only (Imager channel 3 and Sounder channel 11), referred to as the ‘Water Vapour experiment’. Details of the GOES Imager and Sounder instruments may be found in Menzel and Purdom (1994). In these experiments, we assimilate the direct radiances and not retrieved properties or soundings based on these radiances.

The satellite data were processed and remapped to the RAMS grid using the Data Processing and Error Analysis System (DPEAS; Jones and Vonder Haar, 2002). The observation error covariance matrix, **R**, is assumed diagonal with a time-invariant standard deviation set at 2.5 K for each channel. This value was chosen so as to roughly account for both measurement and representativeness errors (Cohn, 1997). It is thus assumed that measurement errors in each channel are not cross-correlated.

The background error covariance matrix, **B**, was developed by Zupanski et al. (2002) and Zupanski et al. (2005). This error is modelled using a spatial, unimodal correlation method and depends on horizontal and vertical decorrelation lengths, and variance, which are assumed time-invariant. These quantities are assumed values based on expected relative error amplitude (e.g. 50% of an average value in a particular vertical layer). The decorrelation lengths and variance were varied and their impacts on the results are discussed in Section 5.

In each experiment presented in this work, RAMDAS was initialized with output from the Final Run (FNL) of the Global Data

Assimilation System (GDAS) reanalysis (Stunder, 1997), and begun at 1100 UTC. GOES observations from 1145 UTC, when the altocumulus cloud was centred over the domain, were assimilated into one 45-min assimilation window and the impacts of the satellite data for one observation time are discussed. The only difference between experiments is in the channels assimilated. No other observations (e.g. temperature, pressure, soundings) are assimilated.

Although this set-up may negate one of the primary benefits of using a 4-DVAR system (i.e. assimilating many observations at different times over successive assimilation windows), it does provide beneficial information toward the military forecasting problem introduced at the beginning of this section. In this context, it is necessary to explore the short-term (or immediate) impact of satellite observations for localized model domains where conventional meteorological observations are not available. The impacts of the satellite data are thus isolated (i.e. not affected by other, non-satellite observations) and the physical response in the model state may be more easily understood.

4. Results

4.1. GOES Imager experiment

The first experiment presented examines the impact of assimilating the water vapour channel (channel 3, 6.7 μm) and infrared window channel (channel 4, 10.7 μm) data from GOES Imager. The values of the observational component of the cost function before (J_0) and after (J_f) assimilation are shown in Table 1, along with the cost associated with each channel. The total cost is the sum of the costs for each channel. This cost is dominated by the channel 4 cost, which is large due to an initial surface temperature error (5–15 K throughout the domain) and lack of clouds in the model. Note, however, that the minimization algorithm is designed to minimize the total cost function, not the cost function for each channel. Thus, the cost associated with channel 3 increases during the assimilation, an increase that is more than offset by the large decrease in cost associated with channel 4.

Table 1. Initial and final values of the observational component of the cost function (J_0 and J_f, respectively) for each experiment. The cost for each channel is also shown

	J_0	J_f
Imager experiment		
Channel 3	1263.7	1893.9
Channel 4	75973.2	20171.8
Total	77236.9	22065.7
Sounder experiment		
Channel 7	29398.9	19722.6
Channel 11	15236.8	11733.9
Total	44635.7	31456.4
Water vapour experiment		
Imager channel 3	1263.7	1075.7
Sounder channel 11	15236.8	13838.5
Total	16500.5	14914.2

The observational cost (second term in eq. (1)) is a weighted sum of the squared differences between the modelled and observed brightness temperatures at each grid point. The minimization algorithm adjusts the initial (1100 UTC) conditions of the model to minimize the difference between the modelled and observed brightness temperatures at the time of the observations (1145 UTC). A comparison of the modelled brightness temperatures to the observations both before and after assimilation demonstrates this (Fig. 4) and explains the trends in the channel-specific cost functions. Initially, the model is much too warm and too dry, and virtually no cloud is present (Figs. 4A and B). After the assimilation, the channel 4 brightness temperatures (Fig. 4D) are reduced throughout the domain, although not enough to match the observed temperature of the cloud (Fig. 4F). The channel 3 brightness temperatures (Figs. 4A and C) are also reduced, most prominently in the southern half of the domain where the observed brightness temperatures are the lowest (Fig. 4E), although they are reduced a little too much (a fact that is reflected by the slight increase in the channel 3 cost over the course of the assimilation).

While the modelled brightness temperatures more closely match the observations, the result of the assimilation is no closer to forming a mid-level cloud. A comparison of the modelled and observed temperature and dew point soundings at North Platte shows that the reduction of brightness temperatures in the window channel (channel 4) is due to a cooling of the surface (Fig. 5B). This cooling of the surface occurs throughout the domain (Fig. 6B) and is between 5 and 15 K throughout the portion of domain over which the cost function is calculated. The surface is cooled until the dew point is reached, resulting the production of fog (Fig. 7B). Note also in Fig. 5B that the atmosphere in the centre of the domain becomes warmer and drier between 1 and 6 km above ground level (AGL), and is cooled and moistened above 10 km AGL. This is not favourable for producing a mid-level cloud. The moistening of the upper-troposphere is more prominent in the southern half of the domain, where the channel 3 brightness temperatures were reduced the most (Fig. 4C).

The assimilation also significantly affected the horizontal and vertical winds (Figs. 8 and 9). The initial surface wind field in the model (Fig. 8A) is qualitatively similar to the observed wind field, although the speeds are biased high. After assimilation, the wind speeds have generally increased and become much more variable in direction (Fig. 8B). The assimilation also increased the vertical velocity (Fig. 9B), replacing the subsidence in the mid-troposphere with updrafts of up to 1.5 m s^{-1}.

The net result of assimilating these GOES Imager channels is that the model cooled the surface, and increased the humidity

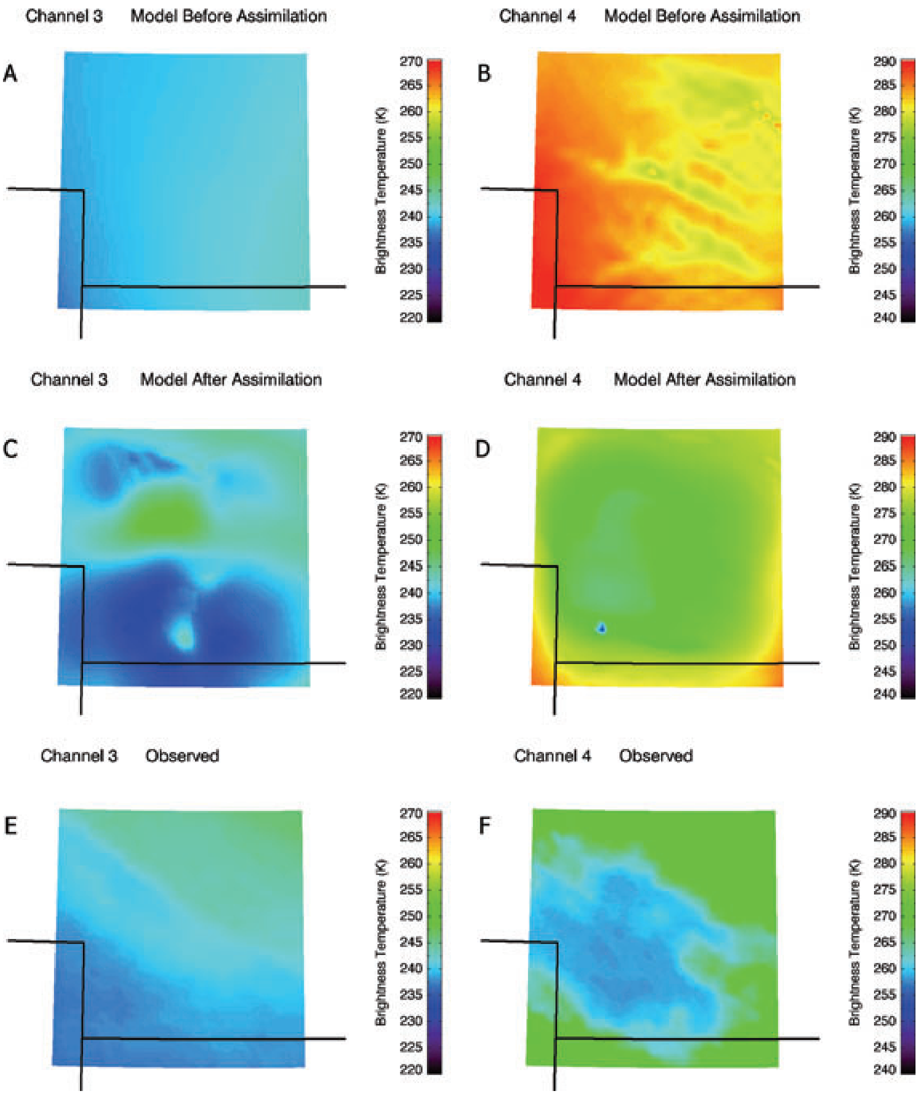

Fig. 4. Comparison between model-simulated brightness temperatures and observed brightness temperatures (Kelvin) for GOES Imager channels 3 and 4 at 1145 UTC 2 November 2001. (A–B) Modelled brightness temperatures for channels 3 and 4 before assimilation. (C–D) Modelled brightness temperatures for channels 3 and 4 after assimilation. (E–F) Observed brightness temperatures from GOES Imager channels 3 and 4. State boundaries are also shown.

in the upper troposphere. This can be explained by the properties of the assimilated channels and of the assimilation system itself. Recall that RAMDAS is designed to handle both clear and cloudy conditions and is strongly constrained (i.e. no model error is assumed). Since the initial model state contains no cloud (except for a few small patches of fog that are 'invisible' to both channels), the adjoint calculates no sensitivity to cloud. In the case of channel 4, when no cloud is present, the highest sensitivity of the brightness temperatures is to the surface temperature. Thus, to minimize the cost, the model cools the surface. This cooling of the surface and lowest kilometre of the atmosphere is limited by the dew point, so that the cooling occurs until saturation is reached and fog is formed. In addition, the increase in upper tropospheric humidity is due to the fact that channel 3 is most sensitive to upper tropospheric humidity. The adjoint-calculated sensitivities are thus constrained to the layers at which the satellite is most sensitive for each of the channels used.

4.2. *GOES Sounder experiment*

The second assimilation experiment explores the use of infrared window and water vapour channels from GOES Sounder. In this case, channel 7 (12.02 μm) is the window channel and channel 11 (7.02 μm) serves as the water vapour channel. Channel 7 has sensitivity to lower-tropospheric humidity and channel 11 is designed to be sensitive to mid-level water vapour (Menzel

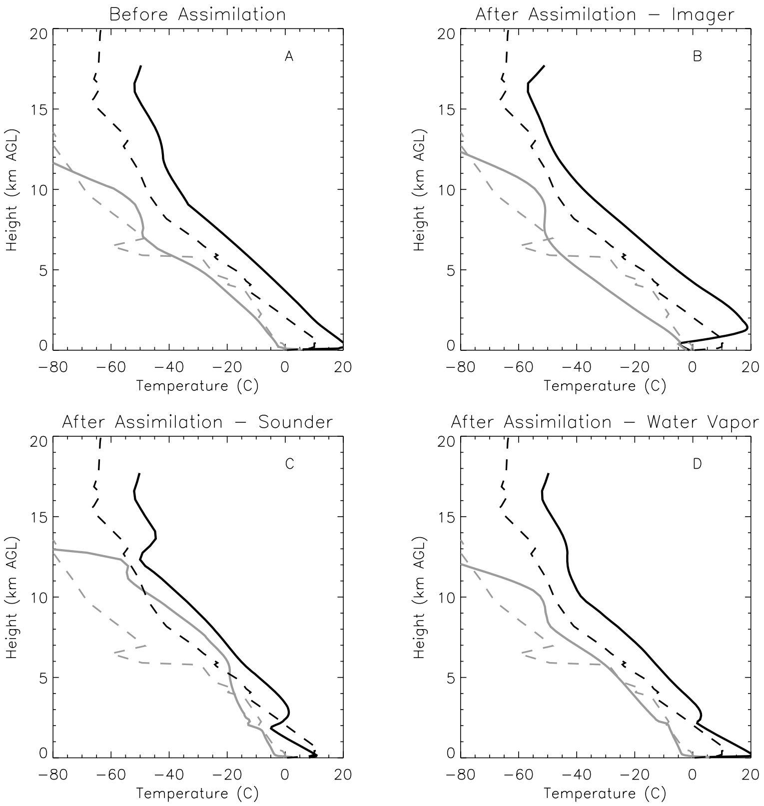

Fig. 5. Model soundings (solid lines) of temperature (black) and dew point (grey) in degrees Celsius at North Platte, Nebraska at 1145 UTC before assimilation (A), and after assimilation of GOES Imager channels 3 and 4 (B), GOES Sounder channels 7 and 11 (C) and GOES Imager channel 3 and Sounder channel 11 (D). In each figure, the observed sounding (dashed lines) from 1200 UTC is shown for comparison.

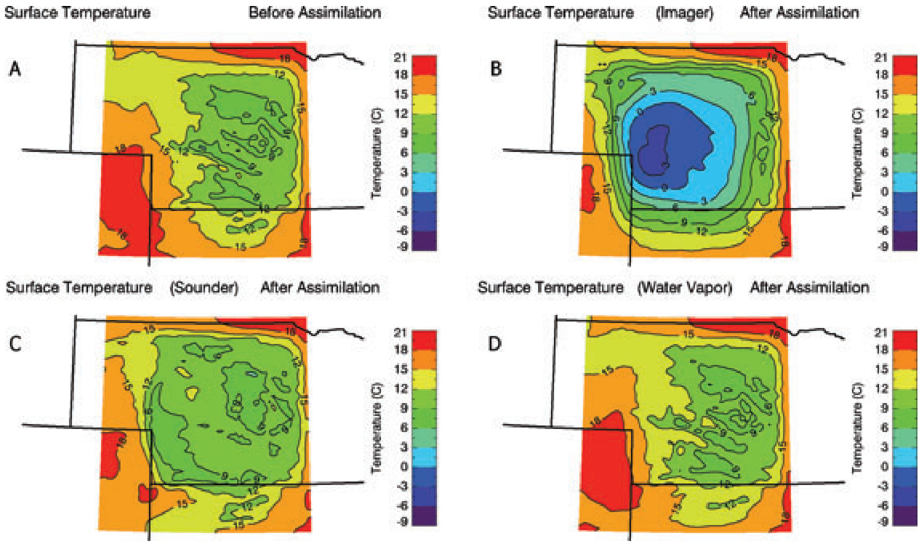

Fig. 6. Model surface temperature in degrees Celsius at 1145 UTC before assimilation (A), and after assimilation of GOES Imager channels 3 and 4 (B), GOES Sounder channels 7 and 11 (C) and GOES Imager channel 3 and Sounder channel 11 (D). State boundaries are also shown.

and Purdom, 1994). This experiment was run exactly as in the GOES Imager experiment above, except in the data that were assimilated.

The values of the observational component of the cost function before and after assimilation are included in Table 1. As with the Imager experiment, the window channel (channel 7) cost dominates the total observational cost, although, in this case, the water vapour channel (channel 11) cost is nearly an order of magnitude larger than in the Imager experiment. This, again, is due to the fact that the model is initially too warm and too dry. However, the total value of the cost function is initially only 58% as large as the cost function for the GOES Imager case,

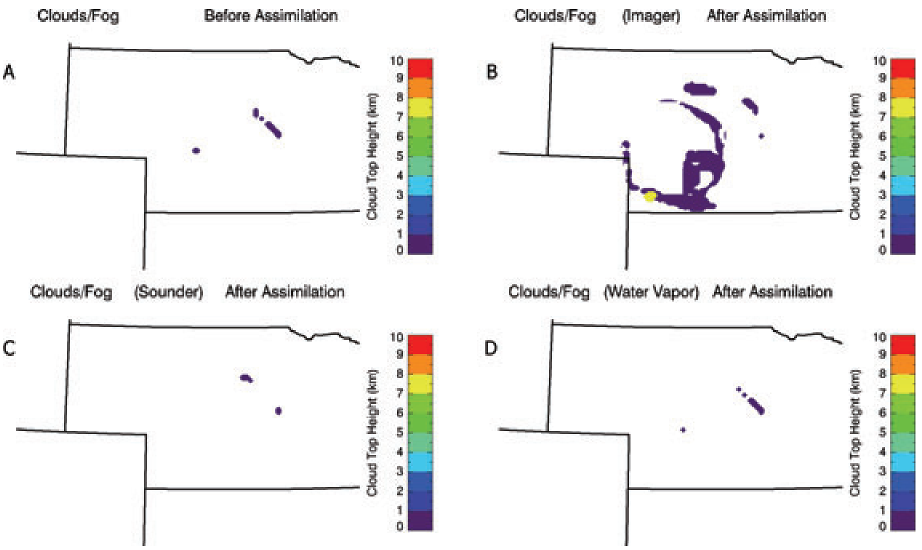

Fig. 7. Model location and height of cloud top (km AGL) at 1145 UTC before assimilation (A) and after assimilation of GOES Imager channels 3 and 4 (B), GOES Sounder channels 7 and 11 (C) and GOES Imager channel 3 and Sounder channel 11 (D). The observed cloud existed between 3.4 and 3.9 km AGL. State boundaries are also shown.

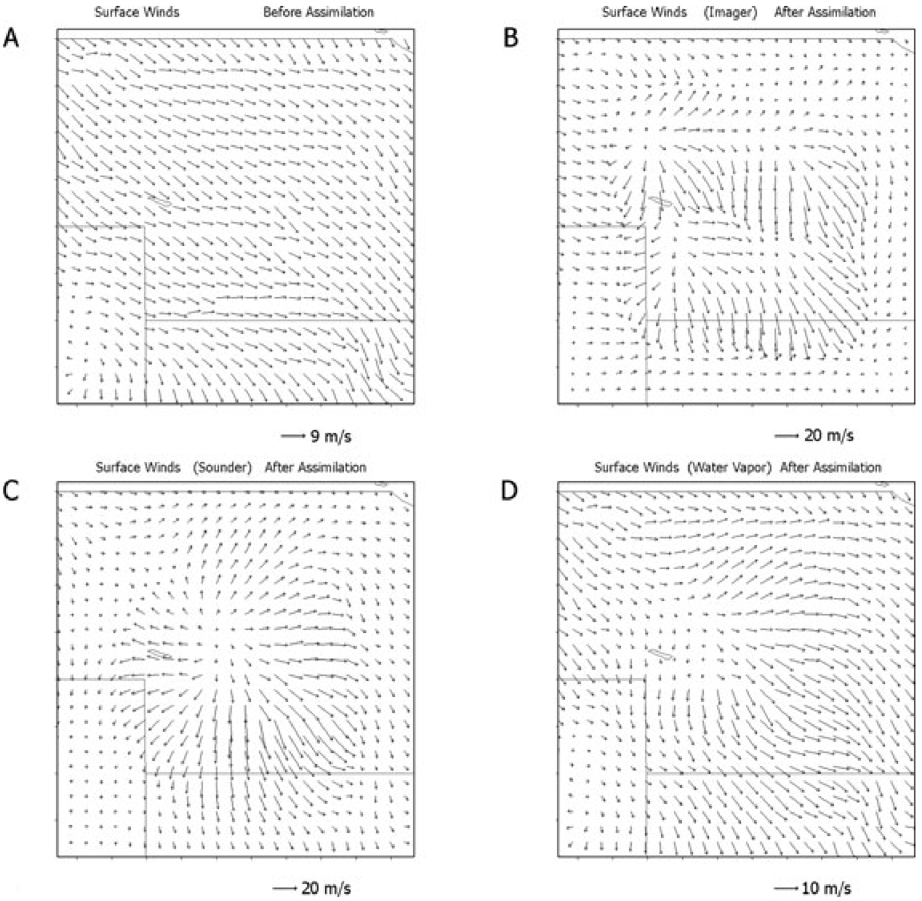

Fig. 8. Model surface wind vectors at 1145 UTC before assimilation (A) and after assimilation of GOES Imager channels 3 and 4 (B), GOES Sounder channels 7 and 11 (C) and GOES Imager channel 3 and Sounder channel 11 (D). Note the change in magnitude of the unit vector in each figure. State boundaries are also shown.

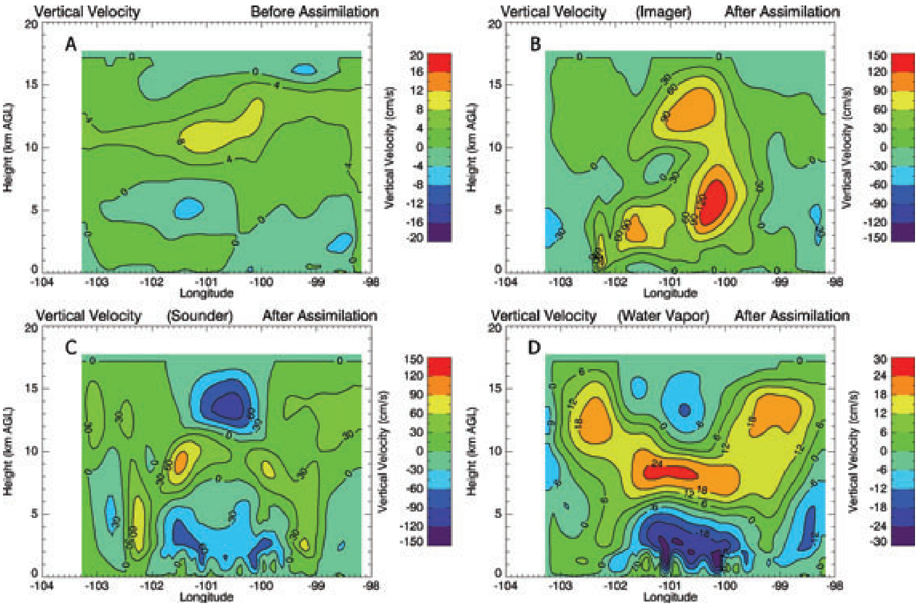

Fig. 9. Vertical-east–west cross-section of vertical velocity (cm s^{-1}) before assimilation (A) and after assimilation of GOES Imager channels 3 and 4 (B), GOES Sounder channels 7 and 11 (C) and GOES Imager channel 3 and Sounder channel 11 (D).

even though the initial model input is identical in both cases, due to differences between the Imager and Sounder channels. After assimilation, the total cost function for the GOES Sounder experiment is 42% larger than in the GOES Imager experiment. As will be shown, the cost function by itself is not an accurate indicator of the quality of the results.

A comparison between the model-simulated brightness temperatures for each channel and the satellite observations at 1145 UTC both before and after assimilation is shown in Fig. 10. Brightness temperatures in both channels start out too high (Figs. 10A and B), reflecting the temperature and humidity errors in the initial forward model run. After assimilation, brightness temperatures in both channels are reduced, particularly in the centre of the domain (Figs. 10C and D), although not to the extent of matching the observations (Fig. 10E and F).

Though the brightness temperature comparison and cost function values indicate that RAMDAS was unable to match the brightness temperatures as well in this experiment as in the Imager experiment, a comparison of meteorological variables shows that this assimilation experiment came much closer to producing a mid-level cloud, particularly in the centre of the domain. Figure 6C shows that the cooling in the window channel (channel 7) is not due to a dramatic decrease in the surface temperatures as in the Imager experiment. The lower brightness temperatures are instead due to the cooling and slight humidifying of the atmosphere near 2 km AGL (Fig. 5C), which produced relative humidity values up to ∼90% in parts of the domain. This layer is approximately 2 km lower than the observed cloud, although it is argued that an attempt to add a cloud in this layer is an improvement over the production of fog. Relative humidity values no greater than 90% are not enough to produce a cloud in this layer, and the assimilation does little with the few patches of fog present in the initial forward model run (Fig. 7C).

The comparison between the post-assimilation sounding with the observed sounding (Fig. 5C) also reveals that this assimilation produced too much moisture between 4 and 13 km AGL near the centre of the domain. The extreme moistening of the mid- and upper troposphere in the centre of the domain in this experiment (as well as the moistening in the Imager and Water Vapour experiments) may be explained as follows. In satellite water vapour channels, such as channel 11 in this case, the brightness temperature is related to the temperature of the primary emitting layer. As the amount of water vapour increases, the emitting layer shifts higher in the vertical, where temperatures are lower, resulting in reduced brightness temperatures. Since the model is 10–15 K too warm (Fig. 5A), the assimilation must add moisture to the mid- and upper-troposphere until the emitting layer moves high enough that the model temperature of that layer is nearly equal to the temperature of the actual emitting layer.

The wind field is also adjusted in interesting ways. Surface winds are changed to a radial pattern, with winds blowing outward from the centre of the domain toward the boundaries of the domain over which the cost function is calculated (Fig. 8C). This results in updrafts along those boundaries and corresponding subsidence in the centre of the domain (Fig. 9C). It is this subsidence that produces the inversion in the sounding near 2 km AGL.

In summary, the primary impacts of assimilating GOES Sounder channels 7 and 11 are: (1) a subsidence inversion is formed near 2 km AGL, resulting in a layer of high relative

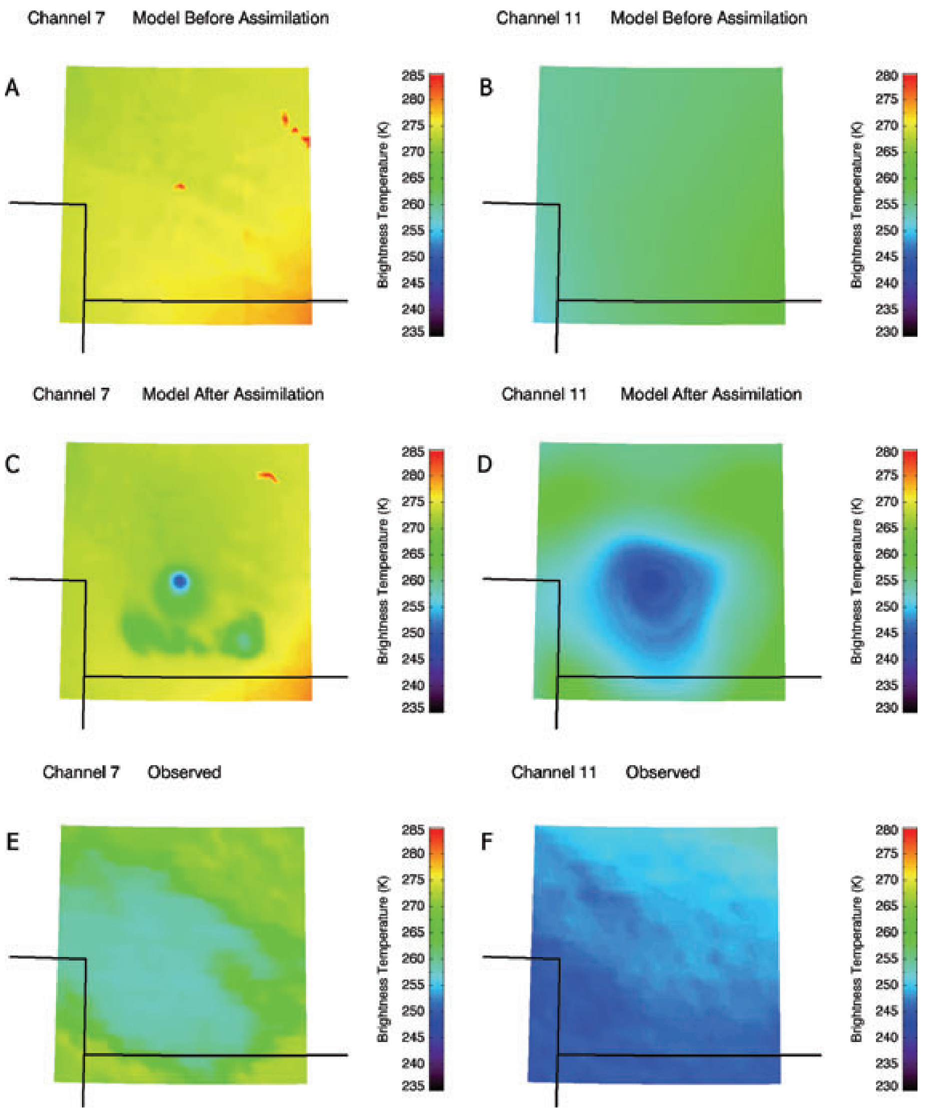

Fig. 10. Comparison between model-simulated brightness temperatures and observed brightness temperatures (Kelvin) for GOES Sounder channels 7 and 11 at 1145 UTC 2 November 2001. (A–B) Modelled brightness temperatures for channels 7 and 11 before assimilation. (C–D) Modelled brightness temperatures for channels 7 and 11 after assimilation. (E–F) Observed brightness temperatures from GOES Sounder channels 7 and 11.

humidity that is much closer to forming a mid-level cloud than the model without assimilation; and (2) the humidity is increased too much between 4 and 13 km AGL in the centre of the domain. The assimilation had less of an effect on the surface temperatures compared to the Imager experiment, and very little effect on the temperature profile above 4 km AGL, as neither channel is particularly sensitive to changes at those levels.

4.3. *Water vapour experiment*

The third experiment of this work utilizes only the two water vapour channels from the previous experiments: GOES Imager channel 3 (6.7 μm) and GOES Sounder channel 11 (7.02 μm). One of the original goals of this work was to determine if assimilating water vapour channel data from satellites would be sufficient to increase the mid-level humidity enough for the model to produce the cloud of 2 November 2001. This experiment tests that hypothesis and allows us to quantify the differences between using only water vapour channels and using a combination of water vapour and window channels as shown in the previous sections.

In this experiment, the initial value of the cost function for each channel is identical to the initial values for these channels shown in each of the previous experiments, due to the fact that the initial model input is identical (Table 1). The total cost function value is considerably less than in the previous experiments since neither channel is sensitive to the large surface temperature error. The temperature error in the mid- and upper-troposphere and

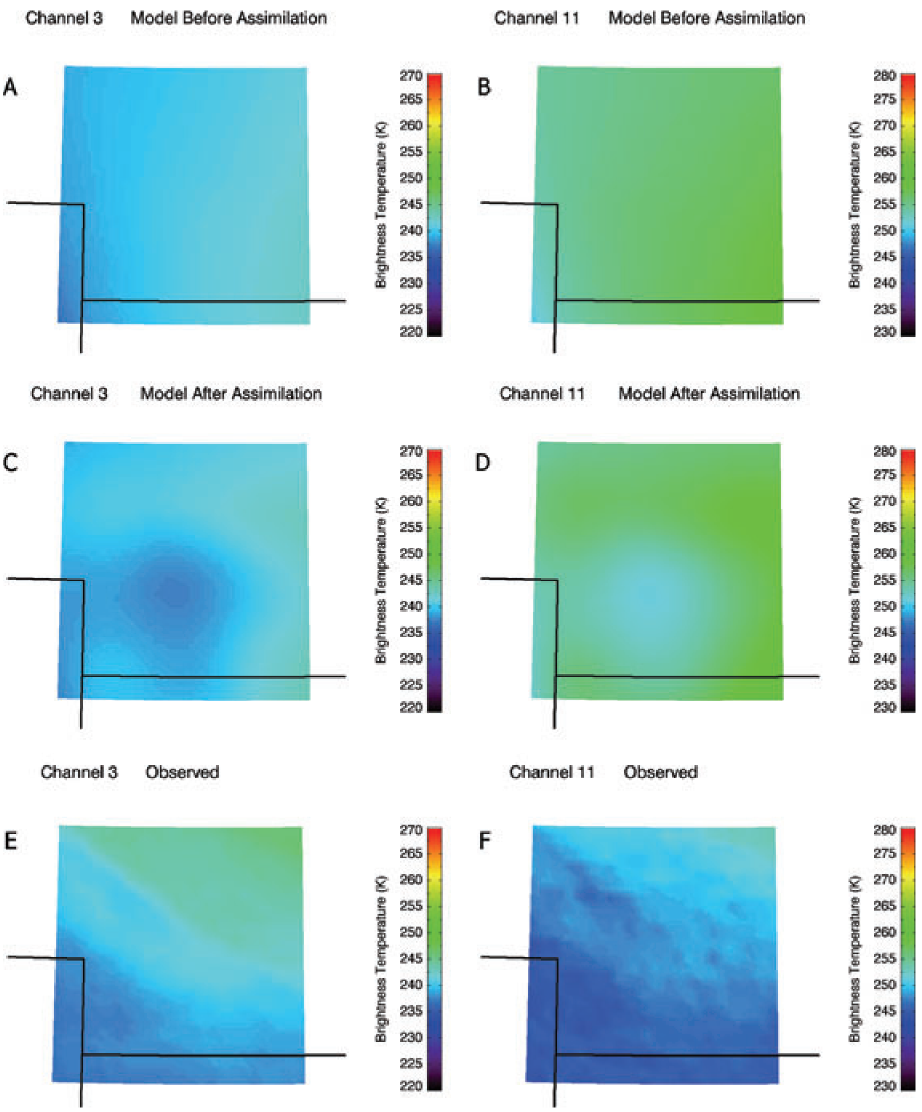

Fig. 11. Comparison between model-simulated brightness temperatures and observed brightness temperatures (Kelvin) for GOES Imager channel 3 and Sounder channel 11 at 1145 UTC 2 November 2001. (A–B) Modelled brightness temperatures for channels 3 and 11 before assimilation. (C–D) Modelled brightness temperatures for channels 3 and 11 after assimilation. (E–F) Observed brightness temperatures from GOES Imager channel 3 and Sounder channel 11.

the dew point error in the upper troposphere (Fig. 5A) combine, and largely offset each other, leading to the lower cost function values.

The results of this experiment are similar to that of the Sounder experiment presented in the previous section, although the impact of the observations is less. The comparison of brightness temperatures with the observations is presented in Fig. 11. This shows that brightness temperatures in each channel were reduced in a ‘bulls-eye’ pattern near the centre of the domain, although to a lesser extent than in the Sounder experiment. The model sounding at North Platte shows that this corresponds to a moistening between 3 and 13 km once again (Fig. 5D). A subsidence inversion is formed near 2 km AGL, but this inversion is not as strong as in the Sounder experiment. The relative humidity does not reach 60% anywhere in the mid-troposphere.

The assimilation induces a similar, but weaker, circulation as in the Sounder experiment (Figs. 8D and 9D). In this case the easterly surface winds induced to the west of the centre point (North Platte) and flowing towards the boundary of the cost function domain cancel out the westerly component of the initial wind field (Fig. 8A), changing the northwest winds to north winds. Similarly, the southerly winds induced north of centre (and northerly winds south of centre) modify the wind field, which sets up a region of subsidence in the lower troposphere at the centre of the domain (Fig. 9D). Rising motions are thus induced on the boundaries of the cost function domain. This circulation results in the subsidence inversion at 2 km AGL.

Apart from the change to the surface winds, the surface remains nearly the same after assimilation. Figure 6D shows that the surface temperature was largely unchanged and Fig. 7D shows the lack of impact on the fog. No other cloud was produced as a result of the assimilation. Since neither water vapour channel is sensitive to the surface, the assimilation of only water vapour channels produces very little impact on surface parameters.

The net result of the assimilation of the two water vapour channels is that the model solution was pushed in the same direction as in the Sounder experiment, although the correction (the change in the model state vector brought about by assimilating the satellite data) was less. The model produced a subsidence inversion near 2 km AGL with a layer of higher relative humidity, but the assimilation was unable to overcome the temperature error in the initial model run. Dew points were increased in the mid- and upper troposphere, but not enough to form a cloud.

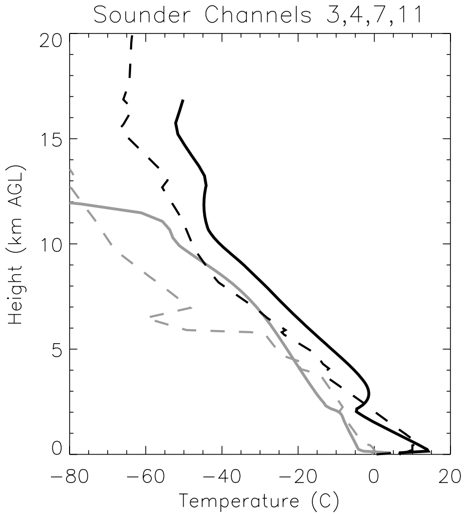

Fig. 12. Model soundings (solid lines) of temperature (black) and dew point (grey) in degrees Celsius at North Platte, Nebraska at 1145 UTC after assimilation GOES Sounder channels 3, 4, 7 and 11. The observed sounding (dashed lines) from 1200 UTC is shown for comparison.

5. Sensitivity of results to model parameters

The experiments presented in the previous section indicate that the assimilation of IR window and/or water vapour channels in a cloud-affected scene was unable to produce a mid-level cloud from an initial model state containing no cloud, given the 4-DVAR algorithm and its configuration presented in Sections 2 and 3. A series of further experiments was run to test the robustness of these results for other configurations of the model and assimilation system. These experiments tested the impact of domain size, decorrelation length and variance (the components of the background error covariance matrix), as well as the use of additional sounding channels. The details and results of these experiments will now be discussed.

5.1. The use of additional GOES Sounder channels

The initial forward model run with no data assimilated poorly handled the 2 November 2001 case study. Temperatures were in error between 5 and 10 K throughout the troposphere (Fig. 5A). It was hypothesized that the use of the mid-level temperature (channel 4, 13.96 μm) and upper-level temperature (channel 3, 14.06 μm) channels from the GOES Sounder instrument would help to constrain the large temperature errors throughout the troposphere in the initial model state and improve the results of the GOES Sounder experiment.

To test this hypothesis, the Sounder experiment was re-run as before with the addition of Sounder channels 3 and 4. The resulting temperature and dew point sounding at North Platte is shown in Fig. 12. The results are similar to those of the original Sounder experiment that excluded channels 3 and 4 (cf. Fig. 12 and Fig. 5C). Once again, a subsidence inversion was produced near 2 km AGL, where relative humidity values were increased to near 90%, but no mid-level cloud was formed. The resulting wind field was similar to the original Sounder experiment.

The similarities between this experiment and the original Sounder experiment are explained as follows. With the presence of a mid-level cloud in the observations, the mid-level temperature channel does not provide information only on the mid-level temperatures, but also on the cloud itself. This is in contrast with microwave channels that may still provide accurate temperature information throughout the column in scenes containing similar clouds. Since the mid-level temperature and window channels are both sensitive to the cloud, they largely provide redundant information. Furthermore, both channels have sensitivity to 2 km AGL in the absence of clouds. With no cloud in the initial model conditions, the adjoint calculates no sensitivity of the total cost to cloud. To reduce the total cost, the system simply reduced the temperatures where both channels (which contributed the most to the total cost) are sensitive to temperature changes (2 km AGL, in this case). The upper-level temperature channel contributed less than 4% of the total cost and had virtually no effect on the results.

5.2. Sensitivity to domain size

As discussed in Section 3, the original experiments (shown in Section 4) used a 450 km × 450 km × 18 km model domain (with 6 km horizontal resolution), masked to 300 km × 300 km × 18 km during calculation of the cost function to prohibit lateral boundary condition errors from influencing the results. The horizontal extent of the outer domain is relatively close to that of the observed cloud (400 × 200 km). It has been suggested that performing the experiments over a larger domain would

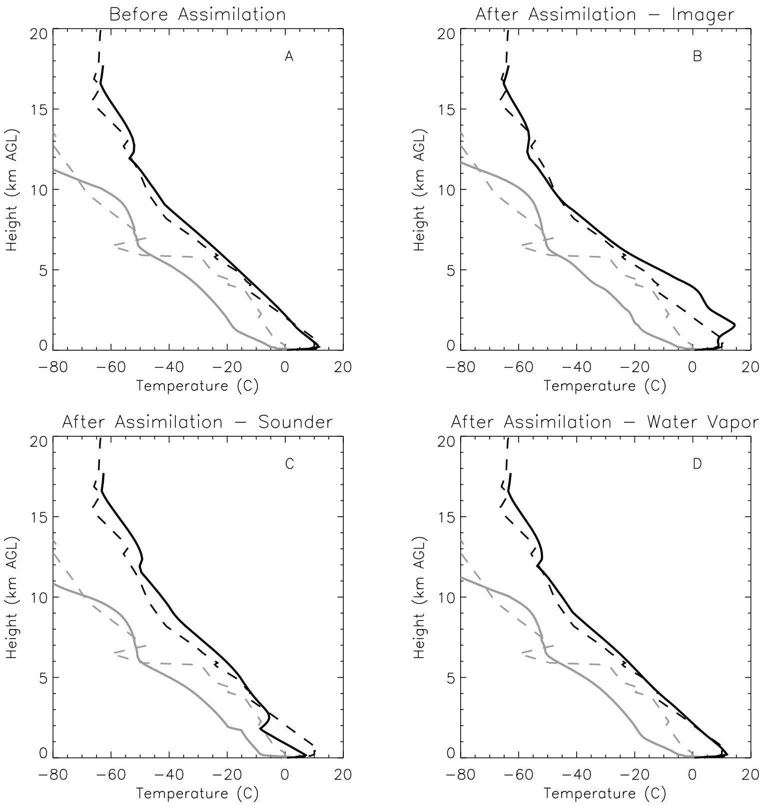

Fig. 13. Model soundings (solid lines) of temperature (black) and dew point (grey) in degrees Celsius at North Platte, Nebraska at 1145 UTC before assimilation (A), and after assimilation of GOES Imager channels 3 and 4 (B), GOES Sounder channels 7 and 11 (C) and GOES Imager channel 3 and Sounder channel 11 (D) using a 600 km × 600 km domain as described in the text. In each figure, the observed sounding (dashed lines) from 1200 UTC is shown for comparison.

positively influence the results. The Imager, Sounder and Water Vapour experiments were re-run using a 600 km × 600 km outer domain masked to 450 km × 450 km during calculation of the cost function. This was the largest domain size that was feasible to test, given limited computational resources. The 6 km horizontal and vertical resolution, time configuration and assimilated channels were not changed from the original experiments shown in Section 4.

The resulting model temperature and dew point soundings at North Platte are shown in Fig. 13 along with the observed radiosonde soundings. Increasing the size of the domain resulted in a decrease in the initial model temperature errors throughout the troposphere and an increase in dew point errors, particularly below 5 km AGL (cf. Fig. 13A and Fig. 5A). The surface temperatures were also reduced by a significant amount (cf. Fig. 14A and Fig. 6A). Despite these changes to the initial model state, the assimilation of each pair of satellite channels produced a similar effect on the model state as happened in the smaller (450 km × 450 km) domain. The Imager channels 3 and 4 cooled the surface (Fig. 14B), warmed the troposphere between 1 and 5 km AGL and increased the upper-tropospheric humidity (Fig. 13B). The cooling of the surface, between 1 and 3 K throughout the domain (Fig. 14B), led to increased fog (not shown). The Sounder channels 7 and 11 produced an inversion near 2 km AGL where the atmosphere was cooled and moistened (Fig. 13C), but not enough to produce a cloud anywhere in the domain. The two water vapour channels (Imager channel 3 and Sounder channel 11) had the smallest effect on the model state, with a decrease in temperature and increase in dew point of less than 1 K between 2 and 5 km AGL (Fig. 13D). In each experiment, the wind field was modified in a manner similar to the experiments performed over the smaller domain, albeit with reduced wind speeds. Except for the additional fog in the Imager experiment, no other clouds were produced as a result of the assimilation experiments.

The values of the observational component of the cost function for each experiment using the larger domain are shown in Table 2. For the Imager and Sounder experiments, these values are smaller than those for the original domain (Table 1), despite the increase in domain size. This is due primarily to the significant reduction in the temperature errors in the initial forward model run. As the surface temperature was reduced throughout the domain, the differences between the observed and model brightness temperatures in the window channels were similarly reduced, greatly reducing the overall observational cost. However, with the surface temperatures still too warm and no cloud in the initial model state, the correction in each experiment occurred in the same direction as in the smaller domain, but with a smaller magnitude change.

Another set of experiments was performed using a 100 km × 100 km domain, centred on North Platte, with 1 km horizontal resolution, utilizing the same pairs of channels. With the entire domain containing cloud and the initial model state cloud-free

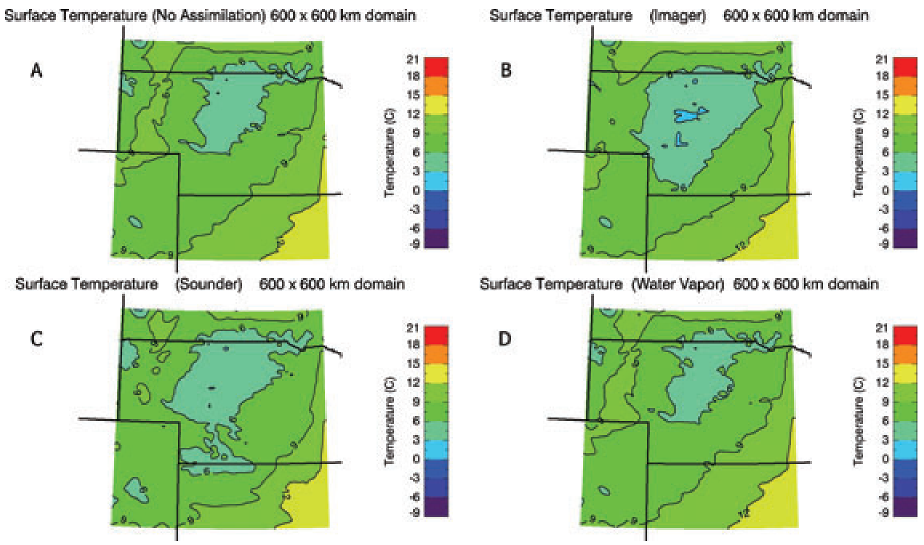

Fig. 14. Model surface temperature in degrees Celsius at 1145 UTC before assimilation (A), and after assimilation of GOES Imager channels 3 and 4 (B), GOES Sounder channels 7 and 11 (C) and GOES Imager channel 3 and Sounder channel 11 (D) using a 600 km × 600 km domain as described in the text. State boundaries are also shown.

Table 2. Initial and final values of the observational component of the cost function (J_0 and J_f, respectively) for each experiment using a 600 km × 600 km domain as described in the text. The cost for each channel is also shown

	J_0	J_f
Imager experiment		
Channel 3	21959.8	19509.2
Channel 4	37210.2	38520.2
Total	59170.0	58029.4
Sounder experiment		
Channel 7	22045.8	19022.6
Channel 11	20619.7	20181.2
Total	42665.5	39203.8
Water vapour experiment		
Imager channel 3	21959.8	23046.3
Sounder channel 11	20630.9	19351.5
Total	42590.7	42397.8

Table 3. Default decorrelation lengths (km) for each of the control variables in RAMDAS. The decorrelation length is the distance over which the correlation between two points in space is reduced to zero. The horizontal decorrelation lengths are given by $r_l^{x,y}$ and the vertical decorrelation lengths are given by r_l^z

Control variable	$r_l^{x,y}$ (km)	r_l^z (km)
Pressure	150	2.0
Temperature	100	2.0
u-Wind	150	2.0
v-Wind	150	2.0
w-Wind	50	1.0
Total water mixing ratio	50	1.0
Rain water mixing ratio	50	0.5
Pristine ice water mixing ratio	50	0.5
Snow water mixing ratio	50	0.5
Aggregate ice water mixing ratio	50	0.5
Graupel mixing ratio	50	0.5
Hail mixing ratio	50	0.5

with temperatures once again 5–15 K too warm, the assimilation system was unable to find a physical solution. In each case, large, unstable perturbations in the model state were produced that the forward model was unable to handle.

5.3. *Sensitivity to background error covariance*

It was discussed in the introduction that the error statistics and uncertainties of the variables in a cloud-resolving model are not well known. In RAMDAS, the background error covariance is based on decorrelation lengths and variance for each of the control variables. The experiments presented in Section 4 used assumed values for the horizontal and vertical decorrelation lengths ($r_l^{x,y}$ and r_l^z, respectively), which are shown in Table 3. A set of experiments was run to determine the impact that changing the decorrelation lengths has on the results of the original experiments by both doubling and halving these decorrelation lengths. The variance was also doubled and halved with very little impact on the results.

Table 4 shows the values of the total observational component of the cost function after assimilation for each of the three main experiments (i.e. Imager, Sounder and Water Vapour) and

Table 4. Final cost function value (J_f) and the ratio of the final cost function value to the initial cost function value (J_0) for each set of data assimilated and each set of decorrelation lengths (r_l)

	Imager Ch. 3 and 4		Sounder Ch. 7 and 11		Imager Ch. 3 Sounder Ch. 11	
	J_f	J_f/J_0	J_f	J_f/J_0	J_f	J_f/J_0
$r_l/2$	55144	0.714	42633	0.955	15703	0.952
Default r_l	22065	0.286	31546	0.707	14914	0.904
$r_l \times 2$	16127	0.209	21119	0.473	12546	0.760

compares them to the cases where the decorrelation lengths presented in Table 3 are halved and doubled. The ratio of the post-assimilation cost function value, J_f, to the pre-assimilation cost function value, J_0, for each of these cases is also shown. In each experiment, the value of the cost function decreases (increases) when the decorrelation lengths are increased (decreased). The observations have more (less) of an impact on the assimilation when the decorrelation lengths are increased (decreased). This may be seen more clearly in Fig. 15, which shows the comparison of the post-assimilation modelled temperature and dew point soundings from North Platte for each set of decorrelation lengths

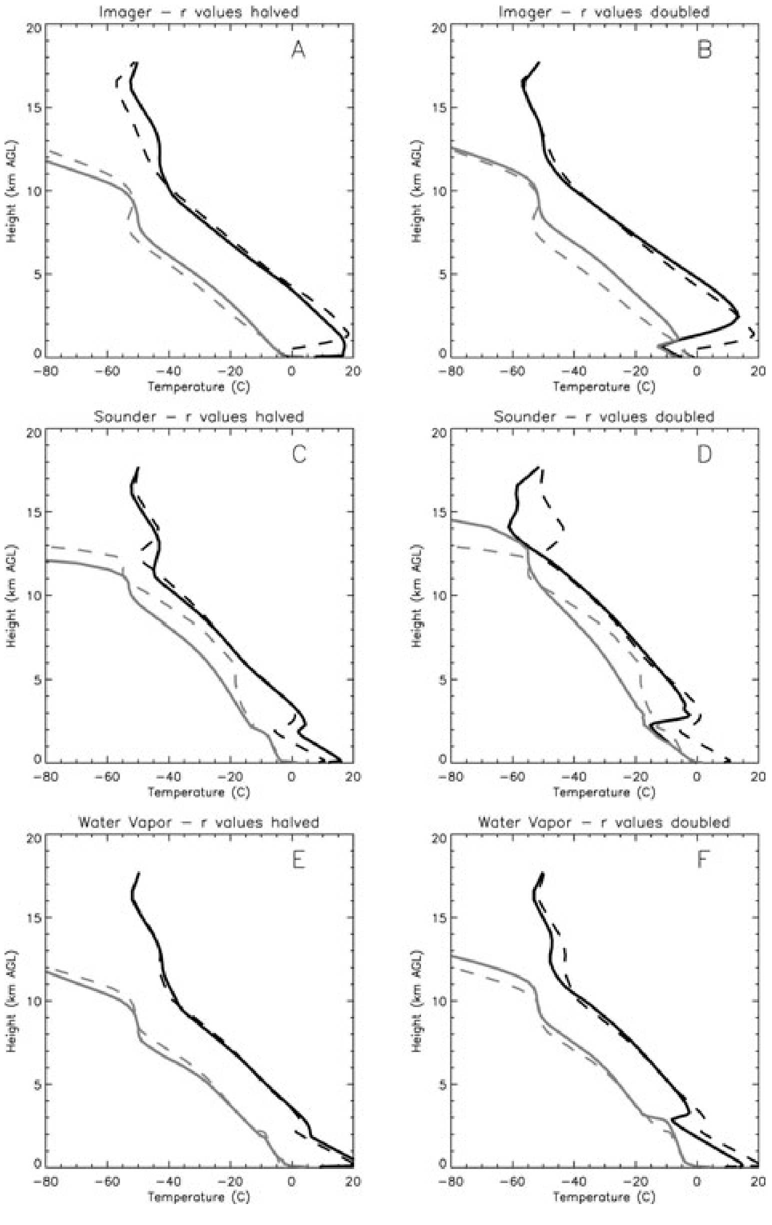

Fig. 15. Model temperature (black) and dew point (grey) soundings from North Platte, after assimilation of GOES Imager ch. 3 and 4 with decorrelation lengths halved (A) and doubled (B), after assimilation of GOES Sounder ch. 7 and 11 with decorrelation lengths halved (C) and doubled (D), and after assimilation of GOES Imager ch. 3 and GOES Sounder ch. 11 with decorrelation lengths halved (E) and doubled (F). In each figure, the dashed lines correspond to model soundings using the default values for the decorrelation lengths.

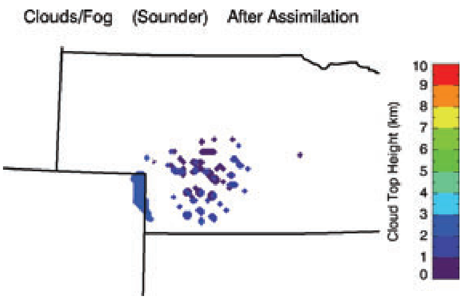
Clouds/Fog (Sounder) After Assimilation

Fig. 16. Model location and height of cloud top (km AGL) after assimilation of GOES Sounder channels 7 and 11 with decorrelation lengths doubled. The largest cloud (along the Nebraska-Colorado border) is the only cloud from any experiment that may be considered 'mid-level', with a top height of 2.5 km AGL. The observed cloud top was 3.9 km AGL.

for the Imager, Sounder and Water Vapour experiments. In each of the three experiments, doubling (halving) the decorrelation lengths increased (decreased) the cooling in the model, which was primarily responsible for the greater (lesser) reduction in cost as a result of the assimilation.

In the case of the Sounder experiment, doubling the decorrelation lengths resulted in the formation of low clouds and clouds above 2 km AGL (Fig. 16). This was the only configuration to produce a cloud that could be considered mid-level.

6. Conclusions

The initial forward model run with no data assimilated poorly handled the 2 November 2001 case study. The observations contained a cold (260 K cloud top), broad, mid-level cloud, while the model contained only a few small patches of fog and a large (5–10 K), warm temperature error throughout the troposphere (Fig. 5A). This led to a large brightness temperature error in both window channels in the model, while the error in the water vapour channels was not as large due to the fact that the model also overestimated the humidity in the mid- and upper troposphere. The observed mid-level cloud existed near 4 km AGL, where the errors in temperature and dew point were $+10$ and -10 K, respectively (Fig. 6A). Subsidence (Fig. 9A) dominated the mid-troposphere in the model as well, which combined with the temperature and dew point errors to prevent a mid-level cloud from forming.

Despite the poor handling of the case by the model, the results of each experiment provide valuable insight into the assimilation of satellite data into a poor initial model state using a strong constraint 4-DVAR technique. Model error was not accounted for as the attempts at developing a linear model error term for RAMDAS (Zupanski, 1997) have not shown any practical benefit in mesoscale satellite data assimilation (Vukićević et al., 2006). Therefore, under the assumption of no model error, the adjoint is told by the forward model that no cloud exists and then calculates sensitivities of the brightness temperatures to model variables under the assumption that there is no cloud. Varying the background error alone was not enough to produce the observed cloud. Other formulations of the model error or other 'weak constraints' have been shown to be a benefit to various assimilation applications (e.g. Watkinson et al., 2007; Trémolet, 2007; Akella and Navon, 2009), however, it is untested whether these constraints would solve the issue addressed here. It is left as a subject for future work.

In each experiment, the assimilation system minimized the cost function by modifying the initial model state as if no cloud were present. With no cloud in the forward model, and thus no sensitivity to cloud in the adjoint, the system modified the surface temperature and upper-tropospheric humidity in the case of GOES Imager channels, as that is what these channels are most sensitive to when no clouds are present. In the case of the GOES Sounder channels, the greatest sensitivities are to low- and mid-level temperatures and mid- to upper-level humidity, which are what were modified by the assimilation. The two water vapour channels have less sensitivity to temperature, so the temperature profile was not modified as much in the water vapour-only experiment as in the previous experiments. In addition, the modelled brightness temperatures in the two water vapour channels were closest to the observations—due to model moisture and temperature errors largely cancelling each other—further reducing the impact of the observations. The correction at the surface was less in the Sounder and Water Vapour experiments as these channels are much less sensitive to surface temperature.

The addition of the mid- and upper-level temperature channels from the GOES Sounder (channels 3 and 4) did not lead to significant improvements over using the window and mid-level water vapour channels alone. The presence of the cloud in the observations limited the temperature information that could otherwise be gained by using the mid-level temperature channel, and thus prevented that channel from properly constraining the large initial temperature errors in the model. In addition, the primary problem still exists that, with no cloud in the initial model state, the system assumes that the cold brightness temperatures are not due to cloud, but instead to cold air at a height near the peak in that channel's sensitivity. The upper-level temperature channel was not a significant contributor to the total cost and had virtually no effect on the assimilation.

Varying the size of the domain had an impact on the results, mostly due to changes in the initial model state. The large temperature errors in the original experiments (using the 450 km × 450 km domain) were greatly reduced using a larger (600 km × 600 km) domain. This lead to smaller impacts from the observations on the model state, although the corrections occurred in the same direction. Note also that, by using a larger domain, the observed cloud represented a smaller proportion of the domain. It is expected that, had the large surface temperature errors still existed in the larger domain, the temperature errors in the cloud-free portions of the domain would exceed the error due to a lack of cloud. This would further inhibit the assimilation system from producing a cloud as the lack of cloud would then be the smaller source of error. When using a very small (100 km × 100 km) domain, the discrepancy between the initial model and the observations was so great that an unphysical correction was produced that the forward model was unable to handle in subsequent iterations.

Decorrelation lengths were found to have a significant impact on the results. Doubling the decorrelation lengths increased the impacts of the observations in each experiment. Halving the decorrelation lengths produced the smallest magnitude changes to the model state in each experiment. It is thought that using the larger decorrelation lengths produced better results in this case because the observed cloud was broad (in the horizontal), and fairly horizontally homogeneous. This is expected to not be the case should this type of experiment be performed on other cloud types that occur on smaller horizontal spatial scales.

Vukićević et al. (2004) and Vukićević et al. (2006) demonstrated that assimilation of cloudy-scene radiances in a similar assimilation framework improves the short-term (0–3 h) model characterization of the cloud when clouds are present in the initial conditions. This work shows that when clouds are absent in the forward model and present in the observations, there is little to no benefit on the model characterization of the cloud—the assimilation modifies the temperature, humidity and winds, rather than the microphysical variables.

While this research focused on a mid-level cloud case, the results are applicable to other forecasting applications. In particular, these results indicate that the most significant changes to the model state by the assimilation are changes that minimize the largest contributors to the total cost function which, in this case, are the sources of the differences between the observed and modelled brightness temperatures. Brightness temperatures, however, are a non-unique function of atmospheric variables. In the infrared window channels, a cloudy scene in one case may have the same brightness temperatures as a cold surface in a different case. It is important for the adjoint to calculate sensitivities to cloud when cloud is present and calculate no sensitivity to cloud when cloud is absent. Additional information is necessary for the adjoint to distinguish between the two scenarios. The observations themselves may be used to provide information on the presence of clouds by way of a cloud mask or cloud top temperature retrieval (e.g. Coakley and Bretherton, 1982), which would provide information to the adjoint on the presence or location of clouds independent of the model.

In addition to a cloud mask, it is clear that further constraints are needed within the system to prevent the system from evolving in a non-physical manner. Recall that the model surface temperature was cooled by 5–15 K during the Imager experiment. This large change in temperature resulted in fog production despite the increase in surface wind speeds up to $\sim$20 m s^{-1} (Figs. 7B and 8B). Furthermore, in each of the Imager experiments, temperatures in the low- to mid- troposphere (generally, between 1 and 6 km AGL) were increased from an initial model state that was already too warm. This is due to the fact that changes in temperature at these levels have very little impact on the cost function given the properties of these Imager channels. Also, the wind circulations induced in order to produce a subsidence inversion and cooling at 2 km AGL in the Sounder and Water Vapour experiments are strongly tied to the boundaries of the model domain, which do not exist in the physical world. More research is needed to develop physical constraints to prevent these types of results. Lipton and Modica (1999) developed a humidity adjustment scheme for the assimilation of cloud-affected visible radiances to help keep the model physically consistent that may provide a starting point. Other physical constraints within the assimilation system (e.g. Jacobs and Ngodock, 2003; Xie et al., 2002; Watkinson et al., 2007) may be beneficial as well.

RAMDAS is based on the common assumption that the errors involved are normally distributed. However, it has been shown that many moisture and cloud variables are not normally distributed and are better represented by a log-normal distribution (Mielke et al., 1977; Miles et al., 2000; Sengupta et al., 2004). The assumption of normally distributed errors for log-normally distributed variables results in the assimilation giving undue weight to model states that are less likely to occur in nature and a non-zero probability for unphysical states, such as negative relative humidity (Fletcher and Zupanski, 2007). Formulations of variational data assimilation theory assuming log-normally distributed variables have recently been derived in Fletcher and Zupanski (2006a,b). It is believed that future studies of cloud-affected radiance data assimilation performed using a log-normal framework would provide more accurate results and may increase the physical robustness of the system.

One of the strengths of a 4-DVAR system is an ability to provide tendency information over multiple observation times. In this work, only one observation time was used. Despite this limitation, it is clear that, under the circumstances presented here, the impact of the two GOES Imager channels used was not favourable for the formation of the observed mid-level cloud and the use of additional observation times would provide no benefit, without the addition of physical constraints to the assimilation system. The GOES Sounder channels appear more likely to produce a mid-level cloud with the use of additional observation times, given the impact present from only one time. However, when this was tested, an unphysical response was initiated within the system similar to that which occurred in the experiments using the very small (100 km × 100 km) domain.

The results presented in this paper suggest that, for success to be achieved using the method employed in this work, more research into the development and use of physical constraints (e.g. those referenced above or new methods entirely) will be needed. The use of conventional meteorological observations (e.g. radiosonde soundings, automated weather station, aircraft and buoy observations), when available within the model domain, may also act as a constraint, depending on how the cost function is defined and the different observation types are weighted. It is expected that the use of non-Gaussian 4-DVAR algorithms as well as improved formulations of the model error and background error covariance will provide a benefit as well.

7. Acknowledgments

This paper was derived from the doctoral dissertation work of Dr. Seaman at Colorado State University. It would not have been possible without the contributions of many individuals who are (or have been) part of the data assimilation research group at CSU/CIRA. In particular, we acknowledge the contributions of Drs. Andrew Jones, Laura Fowler, Tomislava Vukićević (University of Colorado), Milija Zupanski and Dusanka Zupanski, as well as Mr. Scott Longmore and Mr. Adam Carheden, for their efforts in the development and administration of RAMDAS. Dr. Steven Fletcher is recognized for insightful comments and thoughtful discussions in reviewing this work.

The observations used in this research are the result of a major team effort including collaborations with the U.S. Department of Defense and the University of Wyoming. Dr. Lawrence Carey (University of Alabama-Huntsville), Mr. Adam Kankiewicz (WindLogics, Inc.) and the rest of the CLEX-9 research team are recognized for their roles in providing the validation data. This work was supported by the U.S. Department of Defense Center for Geosciences/Atmospheric Research under Cooperative Agreement from the Army Research Laboratory (DAAD19-02-2-0005 and W911FF-06-2-0015).

References

Akella, S. and Navon, I. M. 2009. Different approaches to model error formulation in 4D-Var: a study with high-resolution advection schemes. *Tellus* **61A**, 112–128.

Bauer, P., Lopez, P., Salmond, D., Benedetti, A., Saarinen, S. and Bonazzola, M. 2006. Implementation of 1D+4D-Var assimilation of precipitation-affected microwave radiances at ECMWF. II: 4-Dvar. *Q.J. R. Meteorol. Soc.* **132**, 2307–2332.

Benedetti, A. and Janisková, M. 2008. Assimilation of MODIS cloud optical depths in the ECMWF model. *Mon. Wea. Rev.* **136**, 1727–1746.

Benjamin, S. G., Devenyi, D., Weygandt, S. S., Brundage, K. J., Brown, J. M. and co-authors. 2004. An hourly forecast assimilation cycle: the RUC. *Mon. Wea. Rev.* **132**, 495–518.

Bryant, F. D. and Latimer, P. 1969. Optical efficiencies of large particles of arbitrary shape and orientation. *J. Colloid Inter. Sci.* **30**, 291–304.

Carey, L. D., Niu, J., Yang, P., Kankiewicz, J. A., Larson, V. E. and Vonder Haar, T. H. 2008. The vertical profile of liquid and ice water content in mid-latitude, mixed-phase altocumulus clouds. *J. Appl. Meteorol. Clim.* **47**, 2487–2495.

Coakley, J. A. and Bretherton, F. P. 1982. Cloud cover from high-resolution scanner data: detecting and allowing for partially filled fields of view. *J. Geophys. Res.* **87**, 4917–4932.

Cohn, S. E. 1997. An introduction to estimation theory. *J. Meteorol. Soc. Jpn.* **75**, 257–288.

Cotton, W. R., Pielke, Sr., R. A., Walko, R. L., Liston, G. E., Tremback, C. J. and co-authors. 2003. RAMS 2001: current status and future directions. *Meteorol. Atmos. Phys.* **82**, 5–29.

Cucurull, L., Derber, J. C., Treadon, R. and Purser, R. J. 2008. Preliminary impact studies using global positioning system radio occultation profiles at NCEP. *Mon. Wea. Rev.* **136**, 1865–1877.

Deblonde, G. and English, S. 2003. One dimensional variational retrievals from SSMIS simulated observations. *J. Appl. Meteorol.* **42**, 1406–1420.

Deblonde, G., Mahfouf, J.-F., Bilodeau, B. and Anselmo, D. 2007. One-dimensional variational data assimilation of SSM/I observations in rainy atmospheres at MSC. *Mon. Wea. Rev.* **135**, 152–172.

Deeter, M. and Evans, K. F. 1998. A hybrid Eddington-single scattering radiative transfer model for computing radiances from thermally emitting atmospheres. *J. Quant. Spec. Rad. Trans.* **60**, 635–648.

Evans, K. F. 1998. The spherical harmonics discrete ordinate method for three-dimensional atmospheric radiative transfer. *J. Atmos. Sci.* **55**, 429–446.

Fan, X. and Tilley, J. S. 2005. Dynamic assimilation of MODIS-retrieved humidity profiles within a regional model for high- latitude forecast applications. *Mon. Wea. Rev.* **133**, 3450–3480.

Fleishauer, R. P., Larson, V. E. and Vonder Haar, T. H. 2002. Observed microphysical structure of midlevel, mixed-phase clouds. *J. Atmos. Sci.* **59**, 1779–1804.

Fletcher, S. J. and Zupanski, M. 2006a. A data assimilation method for log-normally distributed observational errors. *Q. J. R. Meteorol. Soc.* **132**, 2505–2519.

Fletcher, S. J. and Zupanski, M. 2006b. A hybrid multivariate normal and lognormal distribution for data assimilation. *Atmos. Sci. Lett.* **7**, 43–46.

Fletcher, S. J. and Zupanski, M. 2007. Implications and impacts of transforming lognormal variables into normal variables in VAR. *Meteorol. Z.* **15**, 1–11.

Garand, L. and Hallé, J. 1997. Assimilation of clear and cloudy sky upper tropospheric humidity estimates using GOES-8 and GOES-9 data. *J. Atmos. Ocean. Tech.* **14**, 1036–1054.

Greenwald, T. J., Hertenstein, R. and Vukićević, T. 2002. An all-weather observational operator for satellite radiance assimilation with mesoscale forecast models. *Mon. Wea. Rev.* **130**, 1882–1897.

Greenwald, T. J., Vukićević, T., Grasso, L. D. and Vonder Haar, T. H. 2004. Adjoint sensitivity analysis of an observational operator for cloudy visible and infrared radiance assimilation. *Q.J. R. Meteorol. Soc.* **130**, 685–705.

Ha, S.-Y., Kuo, Y.-H., Guo, Y.-R. and Lim, G.-Y. 2003. Variational assimilation of slant-path wet delay measurements from a hypothetical ground-based GPS network. Part I: comparison with precipitable water assimilation. *Mon. Wea. Rev.* **131**, 2635–2655.

Harrington, J. Y. 1997. *The Effects of Radiation and Microphysical Processes on Simulated Warm and Transition Season Arctic Stratus*. CSU PhD Dissertation, Colorado State University, Ft. Collins, CO, 289 pp.

Hoffman, R. N., Grassotti, C., Isaacs, R. G., Louis, J.-F. and Nehrkorn, T. 1990. Assessment of simulated satellite lidar wind and retrieved 183 GHz water vapour observations on a global data assimilation system. *Mon. Wea. Rev.* **118**, 2513–2542.

Illingworth, A. J., Hogan, R. J., O'Connor, E. J., Bouniol, D., Brooks, M. E. and co-authors. 2007. Cloudnet. *Bull. Am. Meteorol. Soc.* **88**, 883–898.

Jacobs, G. A. and Ngodock, H. E. 2003. The maintenance of conservative physical laws within data assimilation systems. *Mon. Wea. Rev.* **131**, 2595–2607.

Jones, A. S. and Vonder Haar, T. H. 2002. A dynamic parallel data-computing environment for cross-sensor satellite data merger and scientific analysis. *J. Atmos. Ocean. Tech.* **19**, 1307–1317.

Kalnay, E. 2003. *Atmospheric Modeling, Data Assimilation and Predictability*. Cambridge University Press, Cambridge, UK, 341 pp.

Khairoutdinov, M. F. and Randall, D. A. 2003. Cloud resolving modeling of the ARM Summer 1997 IOP: model formulation, results, uncertainties, and sensitivities. *J. Atmos. Sci.* **60**, 607–625.

Kidder, S. Q. and Vonder Haar, T. H. 1995. *Satellite Meteorology: An Introduction*. Academic Press, San Diego, CA, 466 pp.

Lipton, A. E. 1993. Cloud shading retrieval and assimilation in a satellite–model coupled mesoscale analysis system. *Mon. Wea. Rev.* **121**, 3062–3081.

Lipton, A. E. and Modica, G. D. 1999. Assimilation of visible-band satellite data for mesoscale forecasting in cloudy conditions. *Mon. Wea. Rev.* **127**, 265–278.

Marecal, V. and Mahfouf, J.-F. 2002. Four-dimensional variational assimilation of total column water vapour in rainy areas. *Mon. Wea. Rev.* **130**, 43–58.

McMillin, L. M., Crone, L. J., Goldberg, M. D. and Kleespies, T. J. 1995. Atmospheric transmittance of an absorbing gas, 4. OPTRAN: a computationally fast and accurate transmittance model for absorbing gases with fixed and variable mixing ratios at variable viewing angles. *J. Appl. Opt.* **34**, 6269–6274.

McNally, A. P. 2009. The direct assimilation of cloud-affected satellite infrared radiances in the ECMWF 4D-Var. *Q. J. R. Meteorol. Soc.* **135**, 1214–1229.

McNally, A. P. and Vesperini, M. 1996. Variational analysis of humidity information from TOVS radiances. *Q. J. R. Meteorol. Soc.* **122**, 1521–1544.

McNally, A. P., Derber, J. C., Wu, W.-S. and Katz, B. B. 2000. The use of TOVS level-1B radiances in the NCEP SSI analysis system. *Q. J. R. Meteorol. Soc.* **126**, 689–724.

Menzel, W. P. and Purdom, J. F. W. 1994. Introducing *GOES-I:* the first of a new generation of geostationary operational environmental satellites. *Bull. Am. Meteorol. Soc.* **75**, 757–781.

Meyers, M. P., Walko, R. L., Harrington, J. Y. and Cotton, W. R. 1997. New RAMS cloud microphysics parameterization. Part II: the two-moment scheme. *Atmos. Res.* **45**, 3–39.

Mielke, P. W., Williams, J. S. and Wu, S.-C. 1977. Covariance analysis techniques based upon bivariate lognormal distribution with weather modification applications. *J. Appl. Meteorol.* **16**, 183–187.

Miles, N. L., Verlinde, J. and Clothiaux, E. E. 2000. Cloud droplet size distribution in low-level stratiform clouds. *J. Atmos. Sci.* **57**, 295–311.

Mokhov, I. and Schlesinger, M. E. 1993. Analysis of global cloudiness, part I: comparison of METEOR, Nimbus-7 and ISCCP satellite data. *J. Geophys. Res.* **98**, 12849–12868.

Moreau, E., Lopez, P., Bauer, P., Tompkins, A. M., Janisková, M. and co-authors. 2004. Variational retrieval of temperature and humidity profiles using rain rates versus microwave brightness temperatures. *Q. J. R. Meteorol. Soc.* **130**, 827–852.

Nocedal, J. 1980. Updating quasi-Newton matrices with limited storage. *Math. Comp.* **35**, 773–782.

Pielke, R. A., Cotton, W. R., Walko, R. L., Tremback, C. J., Lyons, W. A. and co-authors. 1992. A comprehensive meteorological modeling system—RAMS. *Meteorol. Atmos. Phys.* **49**, 69–91.

Raymond, W. H., Wade, G. S. and Zapotocny, T. H. 2004. Assimilating GOES brightness temperatures. Part I: upper-tropospheric moisture. *J. Appl. Meteorol.* **43**, 17–27.

Rossow, W. B. and Dueñas, E. N. 2004. The ISCCP web site, an online source for research. *Bull. Am. Meteorol. Soc.* **85**, 167–172.

Ruggiero, F. H., Sashegyi, K. D., Lipton, A. E., Madala, R. V. and Raman, S. 1999. Coupled assimilation of geostationary satellite sounder data into a mesoscale model using the bratseth analysis approach. *Mon. Wea. Rev.* **127**, 802–821.

Ruston, B. C. and Vonder Haar, T. H. 2004. Characterization of summertime microwave emissivities from the Special Sensor Microwave Imager over the conterminous United States. *J. Geophys. Res.* **109**, D19103, doi:10.1029/2004JD004890.

Seaman, C. J. and Vonder Haar, T. H. 2003. *Observed and Calculated Properties of Mid-level, Mixed-phase Clouds*. Masters Thesis, Colorado State University, Fort Collins, CO, 92 pp.

Sengupta, M., Clothiaux, E. E. and Ackerman, T. P. 2004. Climatology of warm boundary layer clouds at the ARM SGP site and their comparisons to models. *J. Clim.* **17**, 4760–4782.

Shanno, D. F., 1985. Globally convergent conjugate gradient algorithms. *Math. Prog.* **33**, 61–67.

Stunder, B. J. B. 1997. NCEP Model Output – FNL Archive Data. TD-6141, National Climatic Data Center. Available online at: http://www.arl.noaa.gov/fnl.php.

Tomassini, M., Kelly, G. and Saunders, R. 1999. Use and impact of satellite atmospheric motion winds on ECMWF analyses and forecasts. *Mon. Wea. Rev.* **127**, 971–986.

Trémolet, Y. 2007. Model-error estimation in 4D-Var. *Q. J. R. Meteorol. Soc.* **133**, 1267–1280.

Tripoli, G. J. and Cotton, W. R. 1982. The Colorado State University three-dimensional cloud/mesoscale model – 1982. Part I: general theoretical framework and sensitivity experiments. *J. Recherches Atmos.* **16**, 185–219.

van Leeuwen, P. J. 2001. An ensemble smoother with error estimates. *Mon. Wea. Rev.* **129**, 709–728.

Vukićević, T., Greenwald, T., Zupanski, M., Zupanski, D., Vonder Haar, T. and co-authors. 2004. Mesoscale cloud state estimation from visible and infrared satellite radiances. *Mon. Wea. Rev.* **132**, 3066–3077.

Vukićević, T. and Paegle, J. 1989. The influence of one-way interacting lateral boundary conditions upon predictability of flow in bounded numerical models. *Mon. Wea. Rev.* **117**, 340–350.

Vukićević, T., Sengupta, M., Jones, A. S. and Vonder Haar, T. H. 2006. Cloud resolving satellite data assimilation: information content of IR window observations and uncertainties in estimation. *J. Atmos. Sci.* **63**, 901–919.

Walko, R. L., Band, L. E., Baron, J., Kittel, T. G. F., Lammers, R. and co-authors. 2000. Coupled atmosphere-biophysics-hydrology models for environmental modeling. *J. Appl. Meteorol.* **39**, 931–944.

Walko, R., Cotton, W. R., Meyers, M. P. and Harrington, J. Y. 1995. New RAMS cloud microphysics parameterization. Part I: the single-moment scheme. *Atmos. Res.* **38**, 29–62.

Warren, S. G., Hahn, C. J., London, J., Chervin, R. M. and Jenne, R. 1986. Global Distribution of Total Cloud Cover and Cloud Type Amount Over Land. NCAR TN-317 STR, 212 pp.

Warren, S. G., Hahn, C. J., London, J., Chervin, R. M. and Jenne, R. 1988. Global Distribution of Total Cloud Cover and Cloud Type Amount Over the Ocean. NCAR TN-317 STR, 212 pp.

Watkinson, L. R., Lawless, A. S., Nicholls, N. K. and Roulstone, I. 2007. Weak constraints in four-dimensional variational data assimilation. *Meteorol. Z.* **16**, 767–776.

Weng, F., 2007. Advances in radiative transfer modeling in support of satellite data assimilation. *J. Atmos. Sci.* **64**, 3799–3807.

Weng, F., Zhu, T. and Yan, B. 2007. Satellite data assimilation in numerical weather prediction models. Part II: uses of rain-affected radiances from microwave observations for hurricane vortex analysis. *J. Atmos. Sci.* **64**, 3910–3925.

Wu, X., Diak, G. R., Hayden, C. M. and Young, J. A. 1995. Short-range precipitation forecasts using assimilation of simulated satellite water vapour profiles and column cloud liquid water amounts. *Mon. Wea. Rev.* **123**, 347–365.

Xie, Y., Lu, C. and Browning, G. 2002. Impact of formulation of cost function and constraints on three-dimensional variational data assimilation. *Mon. Wea. Rev.* **130**, 2433–2447.

Yucel, I., Shuttleworth, W. J., Gao, X. and Sorooshian, S. 2003. Short-term performance of MM5 with cloud-cover assimilation from satellite observations. *Mon. Wea. Rev.* **131**, 1797–1810.

Zapotocny, T. H., Menzel, W. P., Nelson, III, J. P. and Jung, J. A. 2002. An impact study of five remotely sensed and five in situ data types in the Eta data assimilation system. *Wea. Forecast.* **17**, 263–285.

Zupanski, M. 1993. A preconditioning algorithm for large-scale minimization problems. *Tellus* **45A**, 478–492.

Zupanski, M. 1996. A preconditioning algorithm for four-dimensional variational data assimilation. *Mon. Wea. Rev.* **124**, 2562–2573.

Zupanski, D. 1997. A general weak constraint applicable to operational 4DVAR data assimilation systems. *Mon. Wea. Rev.* **125**, 2274–2292.

Zupanski, M., Zupanski, D., Parrish, D., Rogers, E. and DiMego, D. 2002. Four-dimensional variational data assimilation for the blizzard of 2000. *Mon. Wea. Rev.* **130**, 1967–1988.

Zupanski, M., Zupanski, D., Vukićević, T., Eis, K. and Vonder Haar, T. 2005. CIRA/CSU four-dimensional variational data assimilation system. *Mon. Wea. Rev.* **133**, 829–843.